



Research Paper

One-pot microemulsion-mediated synthesis of Bi-rich $\text{Bi}_4\text{O}_5\text{Br}_2$ with controllable morphologies and excellent visible-light photocatalytic removal of pollutants

Danjun Mao, Shanshan Ding, Lingjun Meng, Yuxuan Dai, Cheng Sun*, Shaogui Yang*, Huan He

State Key Laboratory of Pollution Control and Resource Reuse, School of the Environment, Nanjing University, Nanjing, 210023, PR China



ARTICLE INFO

Article history:

Received 28 November 2016

Received in revised form 22 January 2017

Accepted 4 February 2017

Available online 5 February 2017

Keywords:

$\text{Bi}_4\text{O}_5\text{Br}_2$

Emulsion templating

Morphology-controlled

Visible light photocatalysis

O-phenylphenol

ABSTRACT

The novel Bi-rich $\text{Bi}_4\text{O}_5\text{Br}_2$ with tunable morphologies of two-dimensional (2D) nanosheets (NSs), three-dimensional (3D) monodisperse layered microspheres (LMs) and hollow spheres (HSs) have been successfully synthesized via an ionic liquid-in-water (IL/W) microemulsion method. Surfactant TX-100 served as the stabilizer of the IL/W microemulsion, and its concentration significantly influenced the morphology and size of the resulting $\text{Bi}_4\text{O}_5\text{Br}_2$ crystal. Possible formation mechanisms have also been discussed. UV-vis diffuse-reflectance spectra and Density function theory (DFT) calculations indicated that $\text{Bi}_4\text{O}_5\text{Br}_2$ possessed stronger visible light adsorption and more negative conduction band minimum (CBM), which is beneficial to effectively activate molecular oxygen to produce $\bullet\text{O}_2^-$. The photocatalytic activity of Bi-rich $\text{Bi}_4\text{O}_5\text{Br}_2$ with varied shapes was investigated and compared with BiOBr for the removal of fungicide o-phenylphenol (OPP) and antibacterial agent norfloxacin (NOR) and tetracycline hydrochloride (TC) under visible light irradiation. The as-prepared $\text{Bi}_4\text{O}_5\text{Br}_2$ HSs and LMs possess higher photocatalytic efficiency than $\text{Bi}_4\text{O}_5\text{Br}_2$ and BiOBr NSs, which is attributed to the hollow/layered spherical structures and Bi-rich strategies. The $\bullet\text{O}_2^-$ and h^+ are identified to be the major photoactive species during the photo-degradation process by scavenger experiments and EPR methods. This study is expected to provide a stepping stone to purposefully design and explore other novel hollow structures with controllable morphology and enhanced photocatalytic activity.

© 2017 Elsevier B.V. All rights reserved.

1. Introduction

The escalating environment and energy crisis are the most prominent and urgent problem in modern society, which is seriously threatening the existence and development of human [1–3]. Over recent decades, considerable investigations have been drawn to semiconductor-based photocatalysts owing to their potential applications for environmental decontamination and energy conversion [4–7]. At present, the traditional photocatalysts, such as TiO_2 and ZnO , have been widely used for the photocatalytic degradation of pollutants. However, the wide band gap limits their photoactivity to the visible region, making them inefficient for solar light applications [8,9]. Thus, the exploration and application of novel visible-light-driven photocatalysts remains a most essential challenge.

Recently, bismuth oxyhalides (BiOX ($\text{X} = \text{Cl}, \text{Br}, \text{I}$)), originally belong to the Silleín family, have demonstrated excellent photocatalytic activities because of their uniquely layered structure, which features an internal static electric field perpendicular to each layer and facilitates the separation of photogenerated charge carriers [10]. Among all the BiOX samples, BiOBr has attracted wide research interest due to its suitable band-structure and high photocatalytic activity under visible light [11–14]. For instance, Huo's group reported that hierarchical flower-like BiOBr microspheres showed effective photocatalytic activity for the removal of RhB under visible light [15]. However, due to the too positive conduction band minimum (CBM), the photocatalytic activity of BiOBr was still very low for the removal of phenol and its derivatives [16,17]. Density function theory (DFT) calculations of BiOBr indicated that its valence band maximum (VBM) mainly consisted of Br 4p and O 2p orbitals, while the Bi 6p orbitals dominated the conduction band minimum (CBM). The theoretical calculation suggests that an effective way to upshift the CBM position of bismuth oxybromide is to increase content of bismuth. For example, by bismuth-rich strategy,

* Corresponding authors.

E-mail addresses: philasun@126.com (C. Sun), yangsg@nju.edu.cn (S. Yang).

$\text{Bi}_3\text{O}_4\text{Br}$ plates showed much better activity than BiOBr on the photocatalytic degradation of sodium pentachlorophenolate (NaPCP) under visible light [18]. Also, Ye and co-workers reported $\text{Bi}_4\text{O}_5\text{Br}_2$ microspheres displayed a high photocatalytic CO_2 reduction activity under visible light [19]. Therefore, the bismuth-rich strategy would be a good choice to effectively improve the photocatalytic activity of BiOBr .

However, owing to the restricted crystal growth, the controlled synthesis and applications of Bi-rich bismuth oxybromide with tailored morphology and composition is still at their preliminary stages. Up to now, series of synthesis methods have been exploited to prepare Bi-rich bismuth oxybromide particles, such as hydrothermal process [20,21], microwave synthesis [22] and hydrolytic process [19]. The obtained Bi-rich bismuth oxybromide particles present different morphologies including nanosheets, nanobelts and microspheres. As we know, hollow structure is effective during the photocatalytic process, and possesses remarkable features of reduced diffusion resistance, high surface-to-volume ratio, improved accessibility and high photocatalytic activity. Nevertheless, how to obtain the desired hollow structures of Bi-rich bismuth oxybromide to further enhance the photocatalytic activity still needs to be fully exploited.

Herein, for the first time, a novel IL/W microemulsion method was proposed to one-pot synthesis of the monodisperse and morphology-tunable $\text{Bi}_4\text{O}_5\text{Br}_2$ layered microspheres and hollow spheres. In this reaction, the ionic liquid 1-Octyl-3-methylimidazolium bromide ([Omin]Br) could act as Br source, dispersing agent and template simultaneously [23–26]. Moreover, surfactant TX-100 served as the stabilizer of the IL/W microemulsion, which is critical for the formation of layered microspheres and hollow spheres. Interestingly, by the change of the concentration of TX-100, the morphology and size of $\text{Bi}_4\text{O}_5\text{Br}_2$ could be easily regulated. Photocatalytic activities of the $\text{Bi}_4\text{O}_5\text{Br}_2$ layered microspheres and hollow spheres were investigated for the degradation of fungicide o-phenylphenol (OPP), antibacterial agent norfloxacin (NOR) and tetracycline hydrochloride (TC) under visible light irradiation. Moreover, based on the scavenger experiments and EPR analysis, the photocatalytic mechanism of the $\text{Bi}_4\text{O}_5\text{Br}_2$ spheres for OPP degradation was clarified. The close correlation among the band structure, morphology and enhanced photocatalytic property of $\text{Bi}_4\text{O}_5\text{Br}_2$ layered microspheres and hollow spheres were also discussed in details.

2. Experimental section

The o-phenylphenol (OPP), norfloxacin (NOR) and tetracycline hydrochloride (TC) were obtained from Aladdin Reagent Co. LTD. The ionic liquid [Omin]Br (1-Octyl-3-methylimidazolium bromide) (99%) was purchased from Shanghai Chengjie Chemical Co. LTD. All chemicals were of analytical grade and used as received without any further purification.

2.1. Preparation of $\text{Bi}_4\text{O}_5\text{Br}_2$ layered microspheres and hollow spheres

The underlying IL/W microemulsion was established by dissolving a predetermined amount of TX-100 (0, 0.1, 0.2, 0.8 and 2.0 g) as surfactant and 0.56 g ionic liquid [Omin] Br as the oil-phase in 25 mL deionized water. Under vigorous stirring for 3 h a transparent ionic liquid microemulsion was obtained. Thereafter, a yellow homogeneous solution was obtained when 5 mL acidic solutions of $\text{Bi}(\text{NO}_3)_3 \cdot 5\text{H}_2\text{O}$ (2 mmol) was added dropwise into the above IL-microemulsion system. The pH value of the solution was adjusted to 10.5 by adding 2 M NaOH solution. The samples denoted as S-1, S-2 and S-3 represent the ones prepared in the presence of 0, 0.2,

and 0.8 g TX-100, respectively. Afterwards, the solution was stirred for 1 h and transferred to a 50 mL Teflon-lined autoclave, which was placed at 160 °C in an oven for 6 h, and then cooled to room temperature. The product was harvested by filtration and washed with deionized water and ethanol for several times, and dried in vacuum at 60 °C overnight. For comparison, the BiOBr sample was obtained by using the same procedure as S-1 without adding NaOH and labeled as S-0.

2.2. Characterization

The crystalline structures and compositions of samples were determined at room temperature by powder X-ray diffraction (XRD) with Shimadzu XRD-6000 X-ray diffractometer. The scanning electron microscopy (SEM) was carried out by QUANTA FEG 250. Transmission electron microscope images (TEM) were collected from JEM-200CX (JEOL, Japan). X-ray photo-electron spectroscopy (XPS) measurements were performed on a PHI5000 Versa Probe spectrometer with Al-K α radiation (ULVAC-PHI, Japan) to identify the chemical composition and chemical state of the samples. The Brunauer-Emmett-Teller (BET) surface areas were investigated by nitrogen adsorption on a Micromeritics ASAP 2020 N_2 adsorption apparatus. The UV-vis diffuse reflectance spectra (DRS) was recorded on UV-3600 spectrophotometer (Shimadzu, Japan), and pure BaSO_4 was employed as a reference. Electron paramagnetic resonance (EPR) spectra were recorded at room temperature on a Bruker model ESR JES-FA200 spectrometer using spin-trap reagent DMPO (Sigma Chemical Co.) in water and methanol, respectively.

2.3. Photocatalytic activity measurements

The photocatalytic activities were evaluated by the degradation of three different molecular models of pollutants, like OPP, NOR and TC under visible light irradiation, which was performed in a photochemical reactor (XPA-VII, Nanjing Xujiang Electromechanical Plant, China) equipped with a 1000 W Xe lamp with a 420 nm cutoff filter. The relative intensity of the Xenon lamp was measured by an S3000-VIS spectrometer (Hangzhou Seeman Technology Co., Ltd., China), and emission spectrum of Xenon lamp was shown in Fig. S1. The system was cooled with a circulating water bath maintained at room temperature. Experimental details were as follows: 30 mg of the solid catalyst was dispersed into an aqueous solution of OPP (50 mL, 10 mg L^{-1}), NOR (50 mL, 10 mg L^{-1}) and TC (50 mL, 30 mg L^{-1}), respectively. Prior to the irradiation, the solution with the catalyst was sonicated for 10 min and then stirred for 1 h in the dark to allow the system to reach adsorption equilibrium. At given time intervals of illumination, about 3 mL of the suspension was taken out and the solids were subsequently removed from the solution using a 0.22 μm nitrocellulose filter. The concentration of OPP, NOR and TC was determined by UV-vis spectroscopy (UV-1800, Shimadzu, Japan) according to absorbance at 282 nm, 273 nm and 356 nm, respectively.

2.4. Photoelectrochemical measurements

To investigate the photoelectrochemical properties of as-prepared samples, the modified electrodes were prepared as follows: 20 mg of the as-prepared sample was dispersed in 0.3 mL of dimethylformamide under sonication for 1 h to produce a suspension. Then, the resulting slurry was drop-cast onto a piece of ITO slice with a fixed area of 1 cm^2 and allowed to dry under the 120 °C for 10 min. Electrochemical measurements were performed on a CHI760E electrochemical workstation in a standard three-electrode system using the prepared samples as the working electrodes, a platinum wire as the counter electrode, and Ag/AgCl (3 M KCl) as a

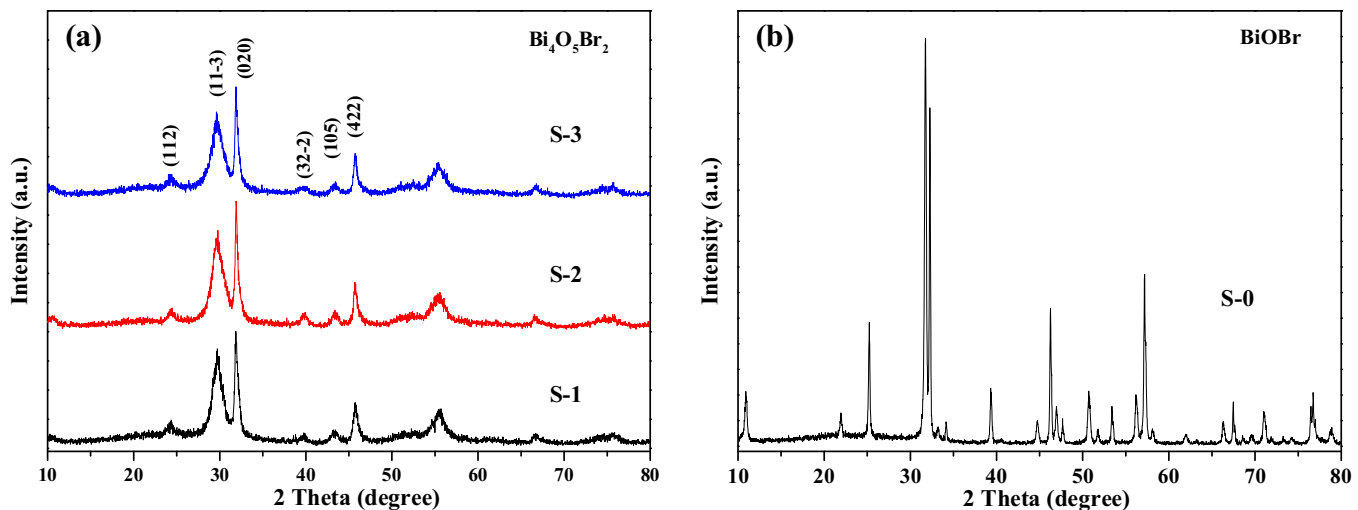


Fig. 1. XRD patterns of as-synthesized $\text{Bi}_4\text{O}_5\text{Br}_2$ samples.

reference electrode. A 500 W Xe arc lamp was utilized as the light source and 0.2 M Na_2SO_4 aqueous solution was used as the supporting electrolyte throughout the photocurrent measurements.

2.5. Theoretical calculations

Density functional theory (DFT) calculations were performed using the plane-wave ultrasoft pseudopotential method with the CASTEP code. The generalized gradient approximation (GGA) in the scheme of Perdew–Burke–Ernzerhof (PBE) formalism was used to describe the exchange and correlation interactions. A plane-wave cutoff energy of 340 eV was employed.

3. Results and discussion

3.1. Catalyst characterization

The phase and composition of the as-prepared samples were examined using powder XRD measurements. Fig. 1a shows the XRD patterns of as-synthesized $\text{Bi}_4\text{O}_5\text{Br}_2$ nanosheets (NSs, S-1), $\text{Bi}_4\text{O}_5\text{Br}_2$ microspheres (S-2) and $\text{Bi}_4\text{O}_5\text{Br}_2$ hollow spheres (S-3) obtained at pH=10.5 with different amounts of TX-100 (0, 0.2 and 0.8 g), respectively. The diffraction peaks of all samples were readily indexed to the monoclinic $\text{Bi}_4\text{O}_5\text{Br}_2$ (space group: P21, unit cell parameters: $a = 1.452$ nm, $b = 0.5625$ nm, and $c = 1.083$ nm,

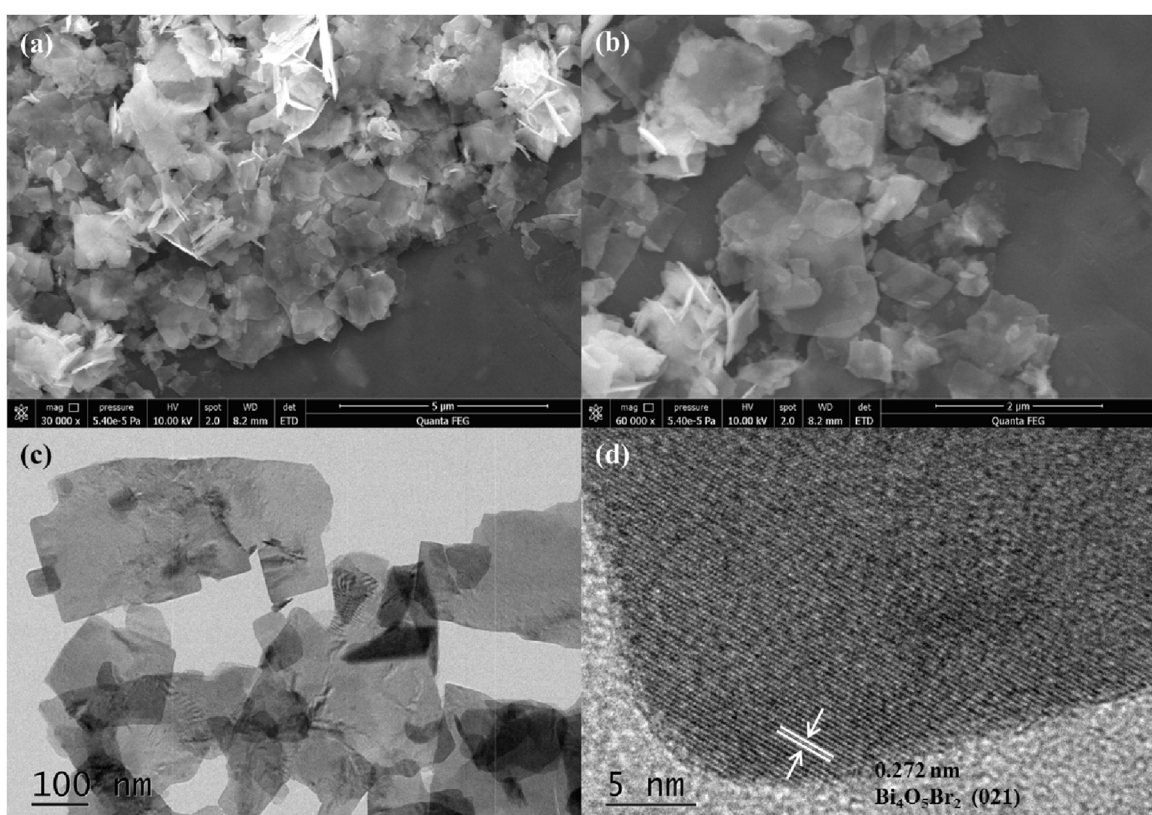


Fig. 2. (a)–(b) SEM images, (c) TEM image and (d) HRTEM image of the as-prepared $\text{Bi}_4\text{O}_5\text{Br}_2$ NSs obtained with no TX-100.

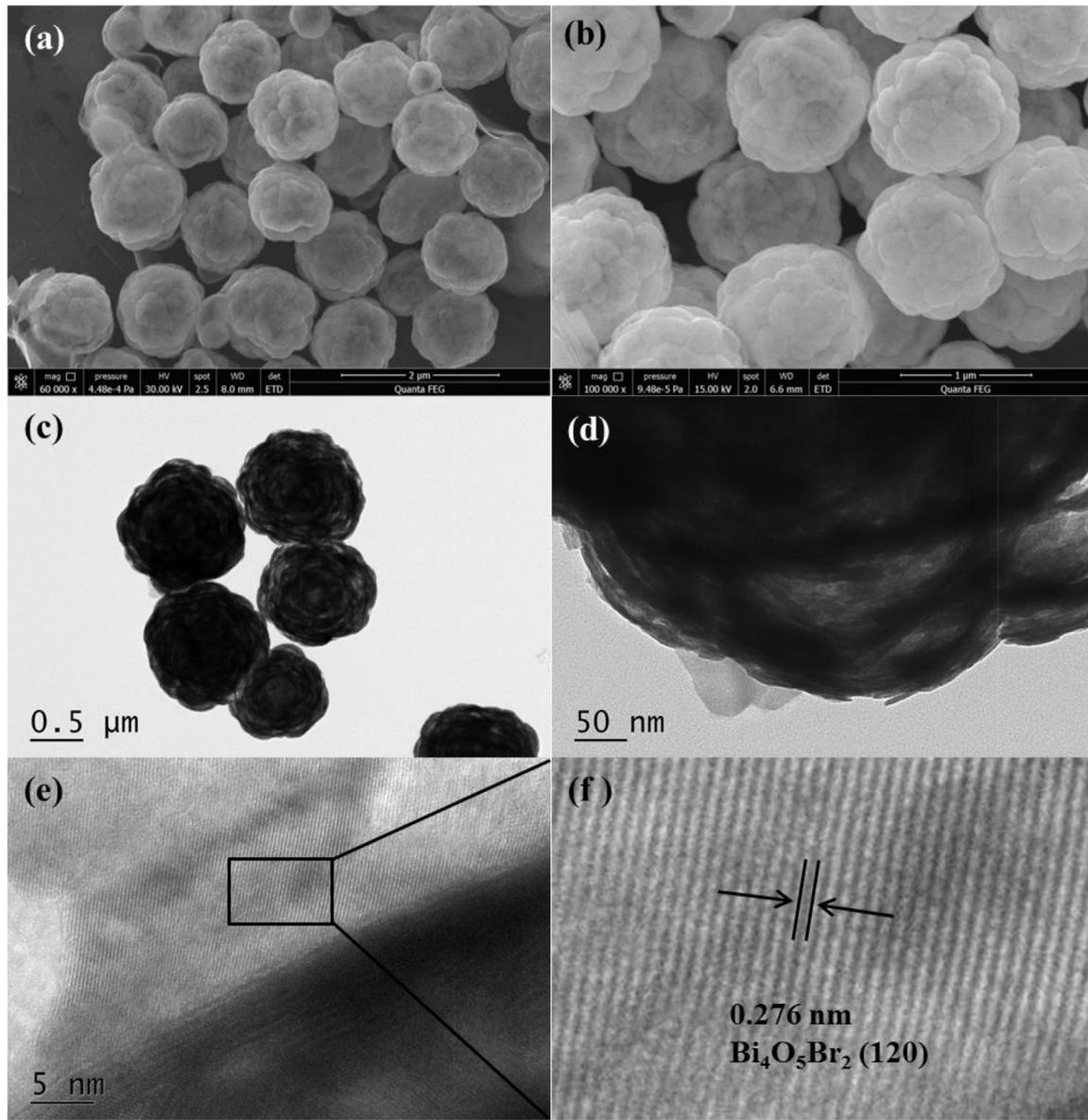


Fig. 3. (a)–(b) SEM images, (c)–(d) TEM images and (e)–(f) HRTEM images of the as-prepared $\text{Bi}_4\text{O}_5\text{Br}_2$ LMs (S-2) in the presence of 0.2 g TX-100.

$\alpha = \gamma = 90.0^\circ$, $\beta = 97.6^\circ$), which match well with the standard XRD data file (JCPDS card no. 37-0699). As shown in Fig. 1b, without adjusting the pH value, the diffraction peaks of the sample were indexed to the tetragonal phase of BiOBr (JCPDS card no. 09-0393). No other peak belonging to impurities is observed, which indicates that all the samples are of a high purity and a single phase.

The microstructures of Bi-rich $\text{Bi}_4\text{O}_5\text{Br}_2$ with varied morphologies of 2D nanosheets, 3D monodisperse layered microspheres and hollow spheres were systematically characterized by SEM and TEM techniques. In the current study, the concentration of surfactant TX-100 has a significant influence on the morphology and size of the resulting $\text{Bi}_4\text{O}_5\text{Br}_2$ crystal. Typical SEM and TEM images of the $\text{Bi}_4\text{O}_5\text{Br}_2$ samples obtained with no TX-100 (S-1) were shown in Fig. 2, from which a large quantity of nanosheets with the size of about 0.5–2 μm were observed. HRTEM image of an individual $\text{Bi}_4\text{O}_5\text{Br}_2$ nanosheet revealed its highly crystalline nature (Fig. 2d). The clear lattice interplanar spacing of 0.272 nm corresponds to the (021) atomic planes of monoclinic $\text{Bi}_4\text{O}_5\text{Br}_2$.

Interestingly, the presence of surfactant TX-100 led to a dramatic change in the resulting morphology. The overall SEM

images of the $\text{Bi}_4\text{O}_5\text{Br}_2$ obtained with 0.1 g of TX-100 are displayed in Fig. S2. It can be seen that the sample consisted of numerous microspheres, but still contained many nanosheets. Further adding TX-100 up to 0.2 g, the monodispersed $\text{Bi}_4\text{O}_5\text{Br}_2$ microspheres with average sizes of $\sim 1.1 \mu\text{m}$ can be obtained (Fig. 3). No other morphologies were observed, indicating a high yield of these microspheres. The TEM images further confirm that the products are layered microspheres and have relatively loose inside (Fig. 3c–d). The typical lattice fringe spacing displayed in Fig. 3e–f was determined to be 0.276 nm, corresponding to the (120) lattice plane of $\text{Bi}_4\text{O}_5\text{Br}_2$.

Fig. 4a and b are the SEM images of the S-3 obtained with 0.8 g of TX-100, which clearly shows a monodispersed and spherical morphology, but the average diameter is declined to about 350 nm. The hollow interior and spherical construction of $\text{Bi}_4\text{O}_5\text{Br}_2$ hollow spheres have also been investigated by TEM images. As displayed in Fig. 4c–d, the hollow nature can be obviously confirmed by the contrast between relatively bright parts with the dark edges. The clear lattice fringe spacing shown in the HRTEM images (Fig. 4e–f) is determined to be 0.289 nm, corresponding to the (113) lattice

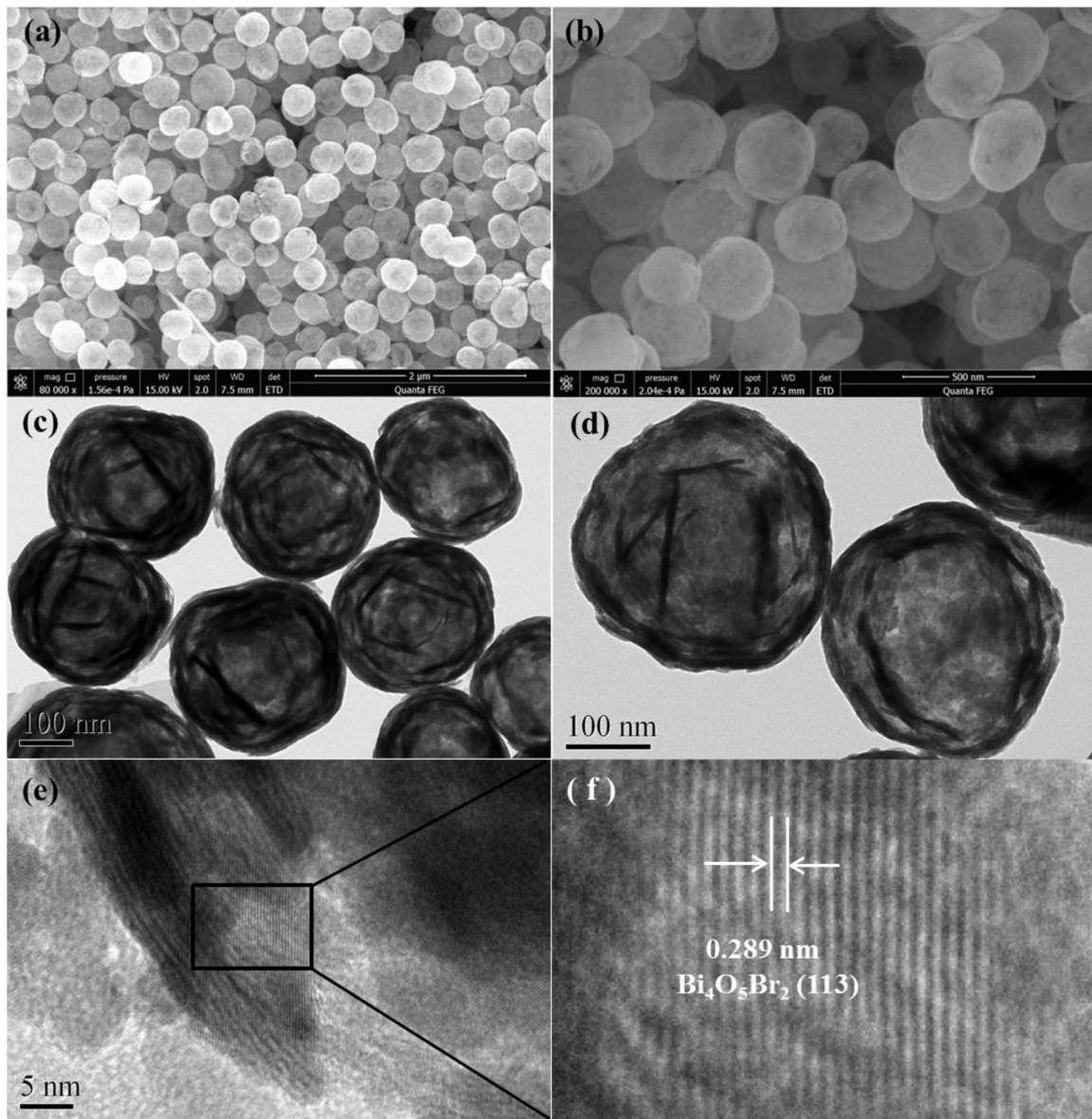


Fig. 4. (a)–(b) SEM images, (c)–(d) TEM images, together with HRTEM images (e)–(f) and SAED pattern (the inset) of the as-prepared $\text{Bi}_4\text{O}_5\text{Br}_2$ HSs (S-3) in the presence of 0.8 g TX-100.

plane of $\text{Bi}_4\text{O}_5\text{Br}_2$. As shown in Fig. S3, when the adding amount of TX-100 was further increased to 2.0 g, the products appeared many nanosheets along with the submicron-scale hollow spheres. For comparison, the BiOBr sample (S-0) obtained without adding NaOH was also shown in Fig. S4. The SEM and TEM images demonstrated that BiOBr sample consisted of plenty of irregular sheets with the size of 1~3 μm .

To gain insight regarding the microstructure and composition of the as-prepared products, chemical element mapping analysis was performed using SEM with EDS. As displayed in Fig. 5a, the elements including bismuth, bromide and oxygen of $\text{Bi}_4\text{O}_5\text{Br}_2$ hollow spheres are homogeneously distributed over the samples. Moreover, the chemical composition of $\text{Bi}_4\text{O}_5\text{Br}_2$ hollow spheres and BiOBr nanosheets was further confirmed by EDS analyses (Fig. 5b and c). It was observed that the Bi/Br atom ratio of $\text{Bi}_4\text{O}_5\text{Br}_2$ and BiOBr was approximately equal to 2:1 and 1:1, respectively. These results were consistent with their theoretical value and XRD results.

In order to further confirm the chemical composition and analyze surface chemical states of BiOBr nanosheets and $\text{Bi}_4\text{O}_5\text{Br}_2$

hollow spheres, XPS analysis was carried out. The binding energies obtained in the XPS analysis were corrected for specimen charging by referencing the C 1 s line to 284.6 eV. As shown in Fig. 6a, both BiOBr and $\text{Bi}_4\text{O}_5\text{Br}_2$ catalysts consist of the Bi, O Br and C elements without existence of other impurity element. Fig. 6b shows the two symmetric peaks of $\text{Bi} 4f_{7/2}$ and $\text{Bi} 4f_{5/2}$ were at 159.1 and 164.4 eV or 158.7 and 163.9 eV in the high-resolution Bi 4f, which can be attributed to Bi^{3+} in BiOBr or $\text{Bi}_4\text{O}_5\text{Br}_2$. Compared to the peaks of BiOBr , the shift of Bi 4f peaks to lower binding energy reveals the different chemical environment of Bi^{3+} in the $\text{Bi}_4\text{O}_5\text{Br}_2$ sample, which was consistent with the theoretical calculation results [18,27,28]. The O 1 s peak binding energy for BiOBr and $\text{Bi}_4\text{O}_5\text{Br}_2$ was centered at 529.9 eV and 529.6 eV, respectively (Fig. 6c). This indicated O atom in the $\text{Bi}_4\text{O}_5\text{Br}_2$ and BiOBr samples was O^{2-} arisen from lattice oxygen. Meanwhile, the binding energy of 68.4 eV associated with Br 3d peak of BiOBr (Fig. 6d), and Br 3d peak of $\text{Bi}_4\text{O}_5\text{Br}_2$ displayed at 68.1 eV with 0.3 eV shift comparing with BiOBr . Moreover, the atomic ratio of Bi: O: Br was about 2.03: 3.26: 1 according to the XPS analysis, which is near to the theoretical value for $\text{Bi}_4\text{O}_5\text{Br}_2$.

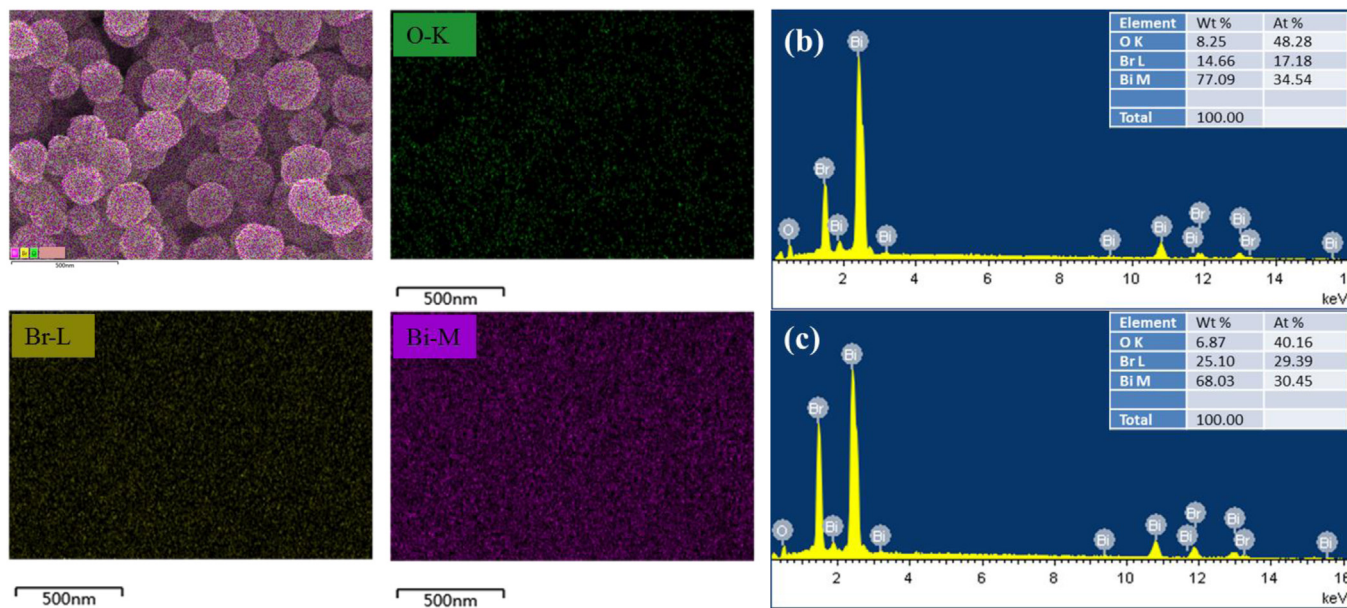


Fig. 5. The elemental mapping (a) and EDS data (b) of $\text{Bi}_4\text{O}_5\text{Br}_2$ HSs; EDS data (c) of BiOBr NSs.

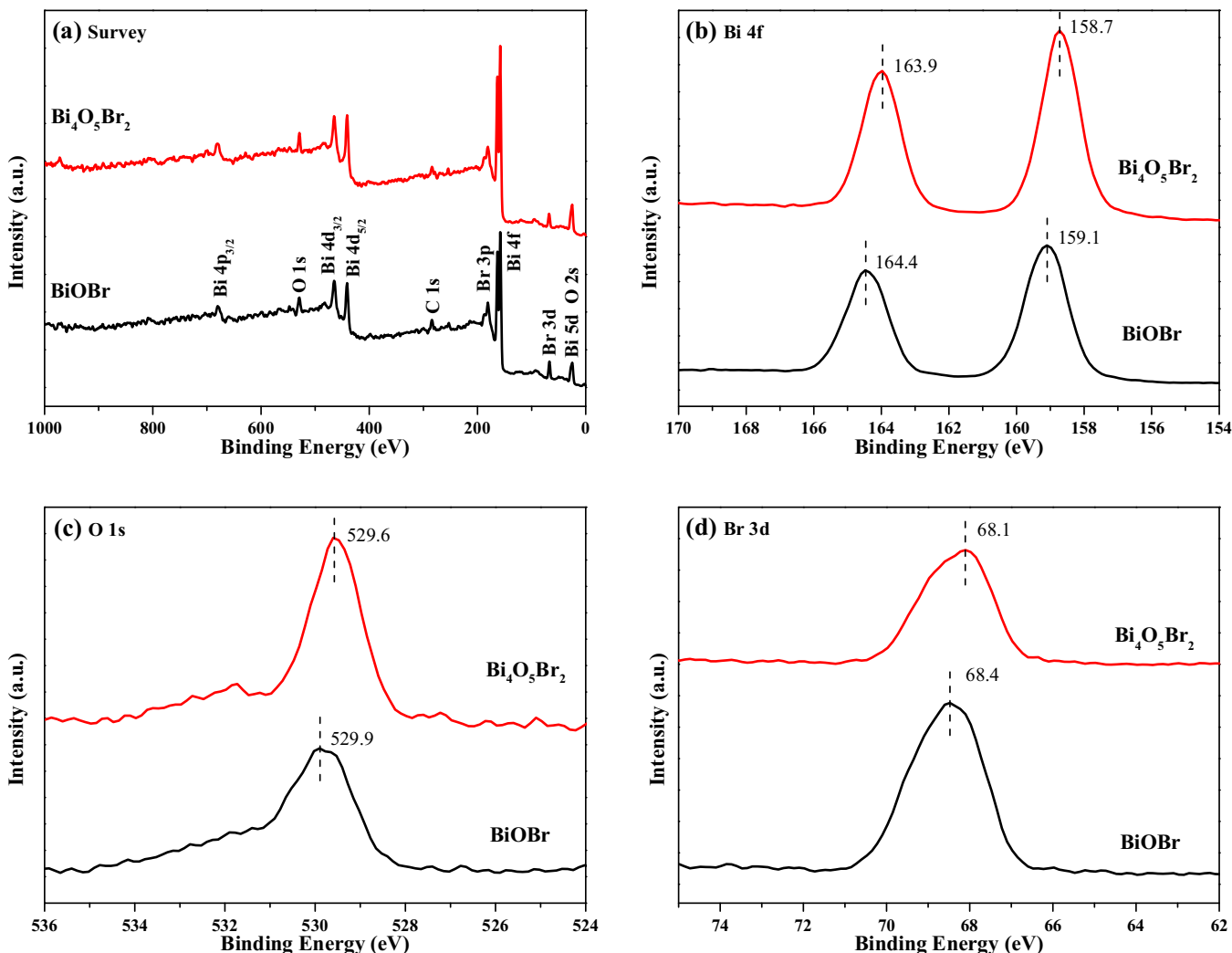


Fig. 6. XPS spectra of the $\text{Bi}_4\text{O}_5\text{Br}_2$ HSs and BiOBr NSs. (a) Survey of the samples; (b) Bi 4f; (c) O 1s; and (d) Br 3d.

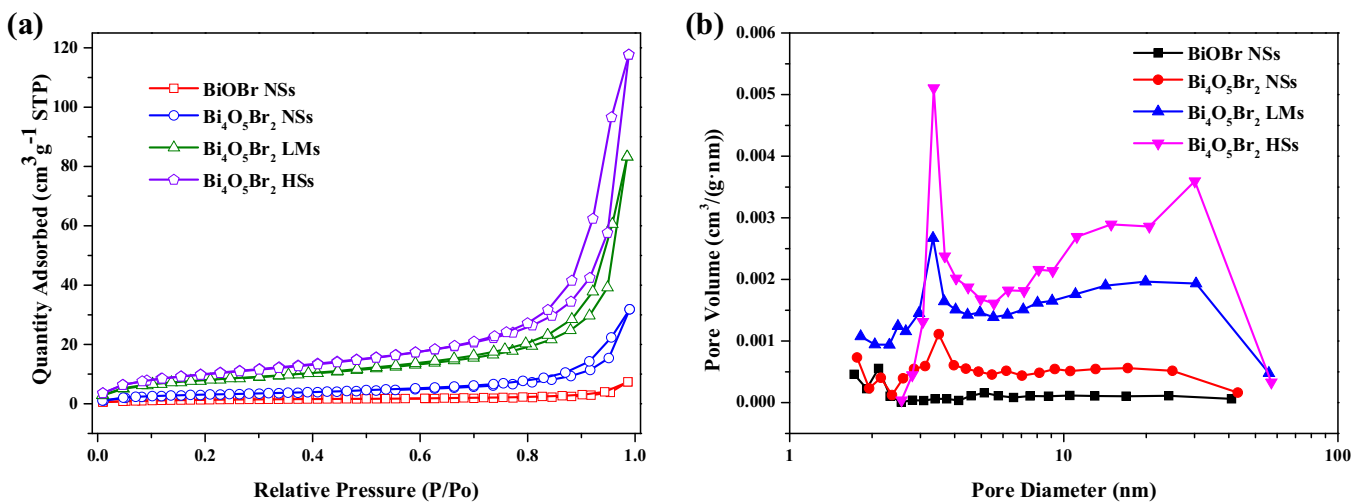
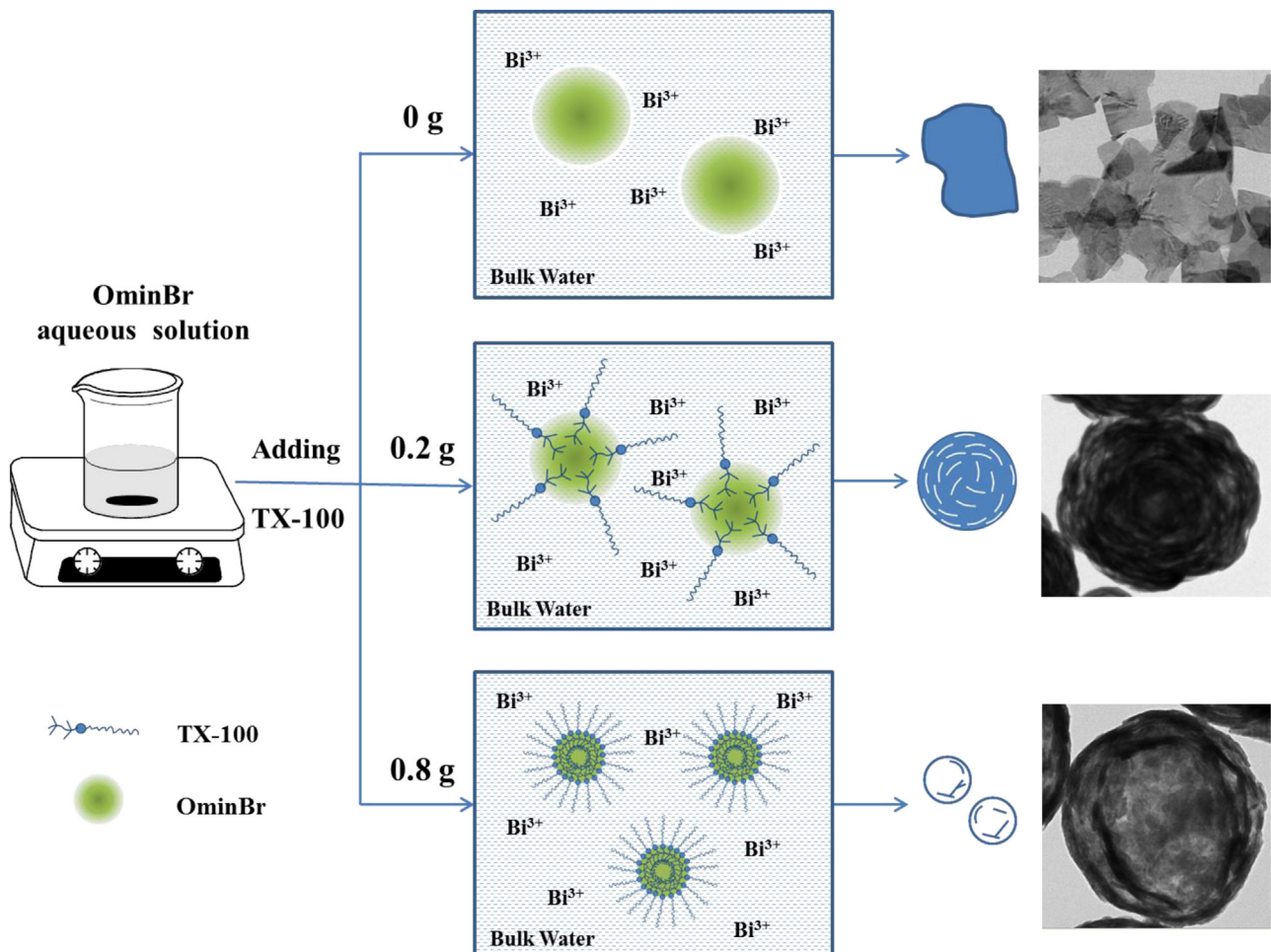


Fig. 7. Nitrogen adsorption-desorption isotherms and pore size distribution curves (inset) of the $\text{Bi}_4\text{O}_5\text{Br}_2$ NSSs (S-1), $\text{Bi}_4\text{O}_5\text{Br}_2$ LMs (S-2) and $\text{Bi}_4\text{O}_5\text{Br}_2$ HSs (S-3).

Combined with the aforementioned results, it can be definitely concluded that the monodisperse bismuth-rich $\text{Bi}_4\text{O}_5\text{Br}_2$ microspheres and hollow spheres have been successfully prepared.

The specific surface area of a semiconductor is considered as one of the main characteristic parameters that affects its photocatalytic efficiency. Fig. 7 describes typical N_2 adsorption-desorption isotherms and their corresponding pore size distributions for the

as-prepared $\text{Bi}_4\text{O}_5\text{Br}_2$ samples. The BET specific surface areas of $\text{Bi}_4\text{O}_5\text{Br}_2$ hollow spheres and layered microspheres were calculated to be $37.53 \text{ m}^2 \text{ g}^{-1}$ and $28.62 \text{ m}^2 \text{ g}^{-1}$, respectively, which were much larger than that of $\text{Bi}_4\text{O}_5\text{Br}_2$ nanosheets synthesized without TX-100 ($10.75 \text{ m}^2 \text{ g}^{-1}$) and BiOBr nanosheets ($7.82 \text{ m}^2 \text{ g}^{-1}$). Moreover, the cumulative pore volume of the $\text{Bi}_4\text{O}_5\text{Br}_2$ hollow spheres, layered microspheres, nanosheets and BiOBr nanosheets determined



Scheme 1. Schematic illustration for the proposed formation process of Bi-rich $\text{Bi}_4\text{O}_5\text{Br}_2$ with different morphologies.

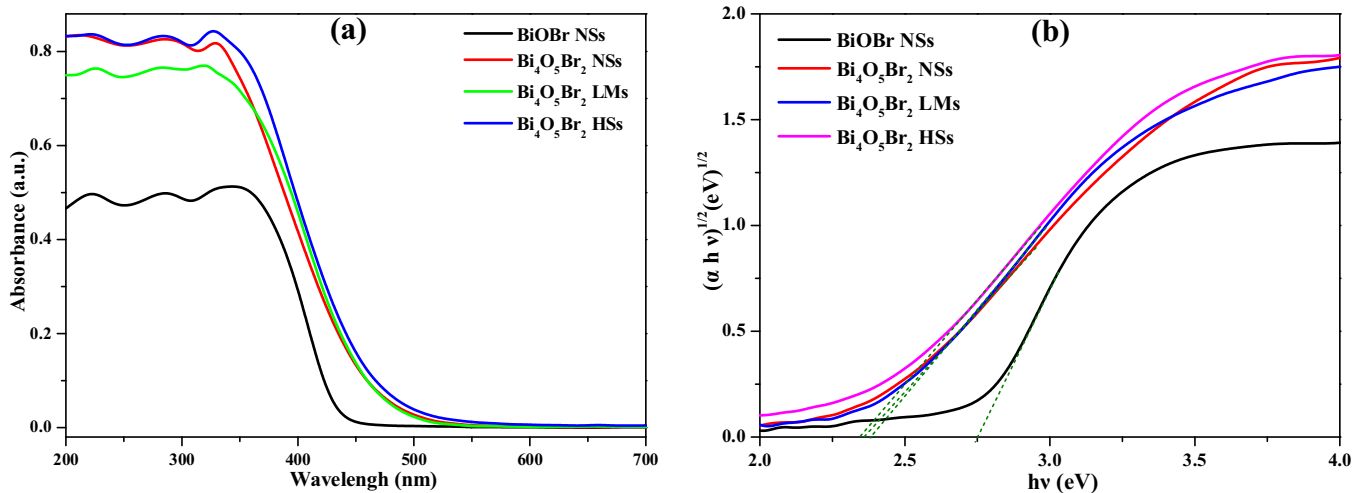


Fig. 8. (a) UV-vis diffuse reflectance spectra; (b) plots of $(\alpha h v)^{1/2}$ vs. photon energy ($h v$) for the as-prepared samples.

with the BJH method was found to be $17.68 \text{ cm}^3 \text{ g}^{-1}$, $12.38 \text{ cm}^3 \text{ g}^{-1}$, $4.74 \text{ cm}^3 \text{ g}^{-1}$ and $1.04 \text{ cm}^3 \text{ g}^{-1}$, respectively. Obviously, $\text{Bi}_4\text{O}_5\text{Br}_2$ hollow spheres and layered microspheres possess larger surface-to-volume ratio, enabling it with more available reaction points.

Thus, $\text{Bi}_4\text{O}_5\text{Br}_2$ hollow spheres and layered microspheres are of high advantages in photocatalytic applications.

The morphology evolution processes of the $\text{Bi}_4\text{O}_5\text{Br}_2$ nanosheets, layered microspheres and hollow spheres are schematically illustrated in Scheme 1. Due to the limited mis-

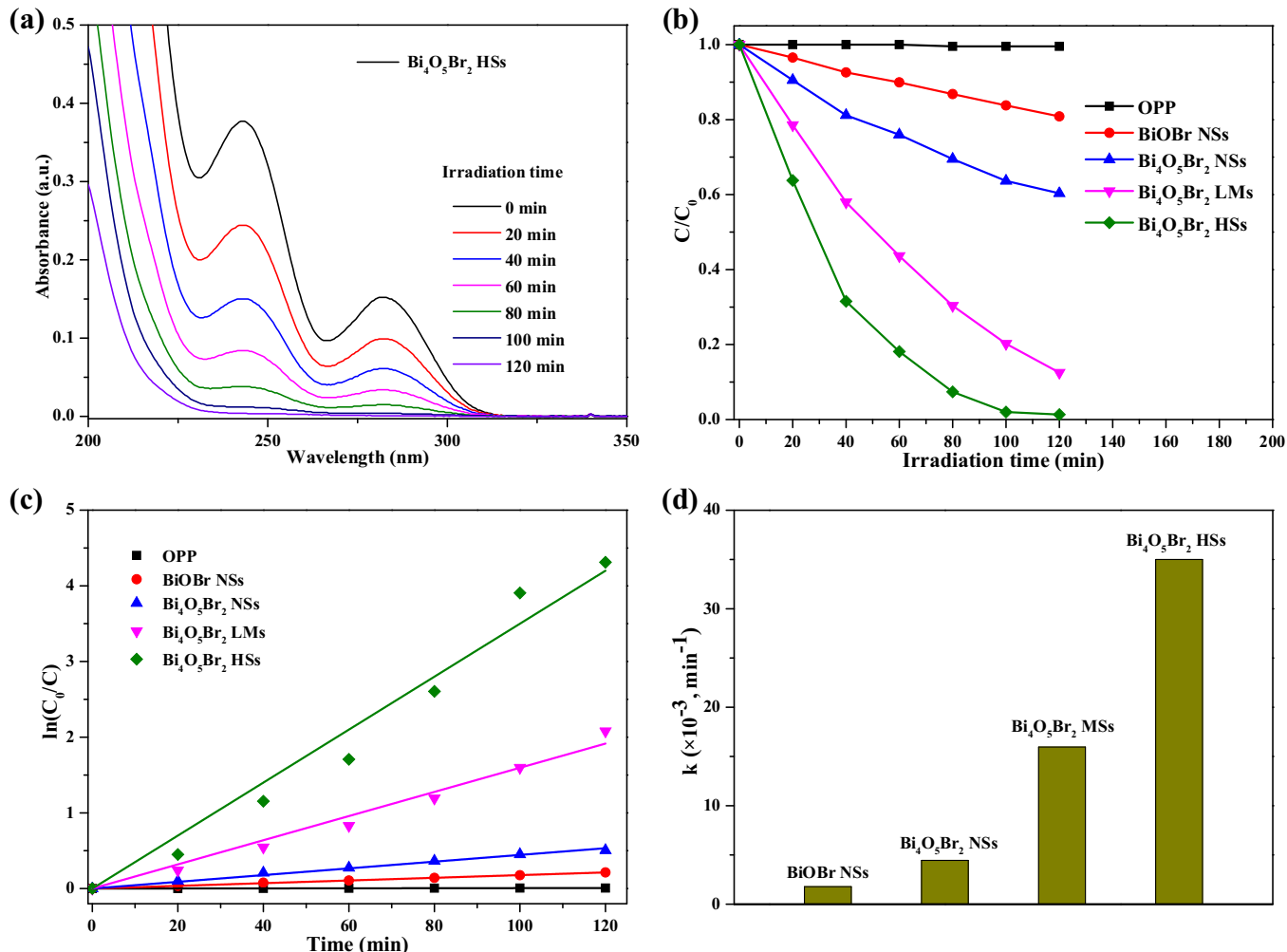


Fig. 9. (a) Temporal UV-vis absorption spectral changes of OPP in the presence of $\text{Bi}_4\text{O}_5\text{Br}_2$ HSs under visible light irradiation; (b) photodegradation curves of OPP over different samples; (c) Linear plots of $\ln(C_0/C)$ vs. degradation time; (d) the degradation rate constants (κ) calculated from c.

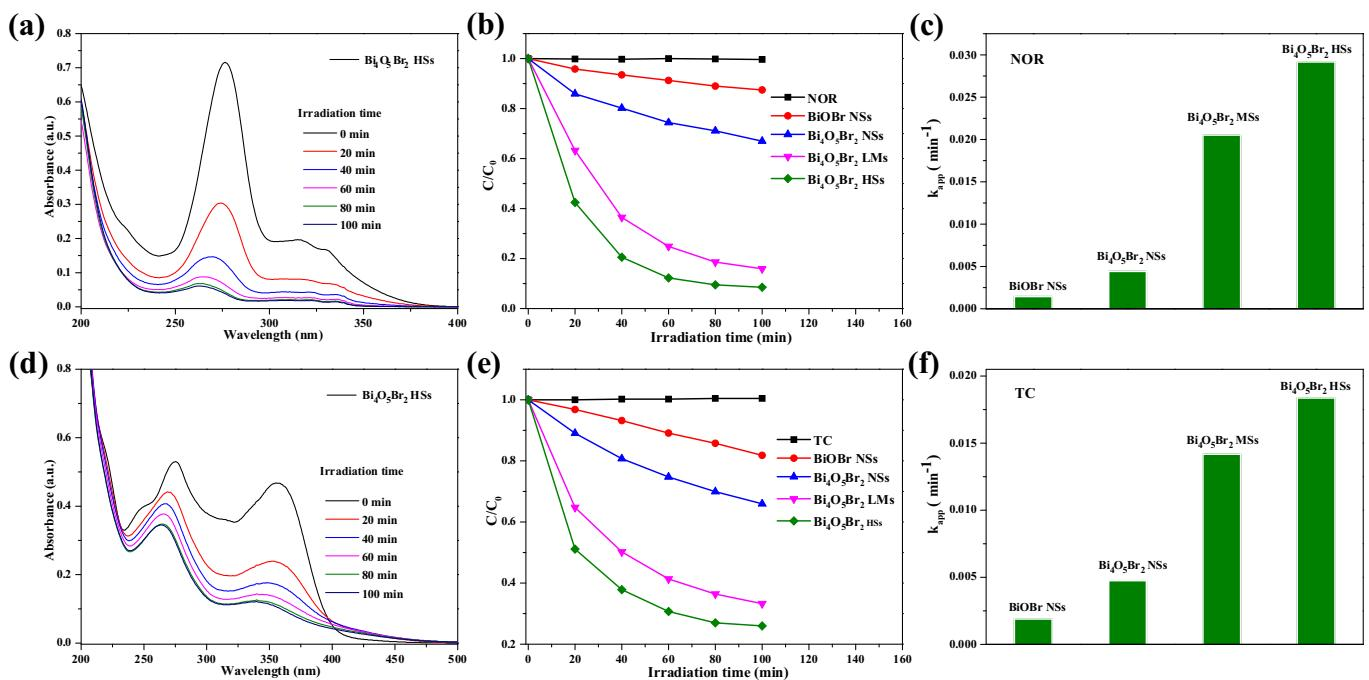


Fig. 10. UV-vis spectra of NOR (a) and TC (d) catalyzed by Bi4O5Br2 HSS under visible light irradiation; photocatalytic degradation of NOR (b) and TC (e) over the as-prepared products under visible light irradiation; the degradation rate constants (k_{app}) calculated from b (c) and e (f).

cibility of the ionic liquid with water, emulsion droplets are formed under vigorous magnetic stirring. The emulsion droplets are susceptible and unstable during the synthesis process [29]. Therefore, only sheet-like structures were formed in the absence of TX-100. However, with the addition of 0.2 g of TX-100, stable ionic liquid/TX-100/water ternary microemulsions were obtained, which can be attributed to the hydrogen bond formation and hydrophobic effect between the ionic liquid and TX-100 [30]. When the Bi³⁺ ions are added dropwise into the ternary system, they will react with [Omin]Br at the interface to form Bi₄O₅Br₂ layered microspheres with relatively loose inside. Further increasing TX-100 can effectively reduce the hydrodynamic diameter of the microemulsions and enhance the ratio of hydrophobic chain of Triton X-100 in the oil (IL)-regions [31]. Thus, submicron-scale hollow spheres may appear as the resulting morphology.

The photocatalytic activity of a semiconductor is closely related to its energy band structure feature. Fig. 8a shows the UV-vis diffuse reflection spectra of the as-synthesized BiOBr nanosheets, Bi₄O₅Br₂ nanosheets, layered microspheres and hollow spheres in the wavelength range of 200–700 nm, respectively. The absorption band-edge of all the Bi₄O₅Br₂ materials was at about 480 nm, which was greater than that of BiOBr (430 nm). These results are consistent with the pale-yellow and yellow colors of BiOBr and Bi₄O₅Br₂ materials, respectively. The corresponding band gap energy of these samples may then be evaluated using the following formula [32,33] $\alpha h\nu = A(h\nu - E_g)^{n/2}$, where α , ν , E_g and A are the absorption coefficient, light frequency, band gap energy, and a constant, respectively, and n depends on the characteristics of the transition in the semiconductor. For Bi-O-Br, n is 4 for its indirect transition. Therefore, the band-gap energy (E_g value) of the products could be estimated from a plot $(\alpha h\nu)^{1/2}$ versus photon energy ($h\nu$). The intercept of the tangent to the x axis will give a good approximation of the band gap energy for the as-synthesized samples, as shown in Fig. 8b. The estimated band gap energies of the BiOBr nanosheets, Bi₄O₅Br₂ nanosheets, layered microspheres and hollow spheres were at 2.75, 2.38, 2.36 and 2.35 eV, respectively. The

above discussion indicated that Bi₄O₅Br₂ can be more effectively excited by visible light and generate more $h^+ - e^-$ pairs, which can promote the photocatalytic reaction.

3.2. Photocatalytic performance

The photocatalytic activity of the synthesized Bi₄O₅Br₂ layered microspheres and hollow spheres was evaluated and compared with the Bi₄O₅Br₂ and BiOBr nanosheets for the degradation of OPP, NOR and TC under the visible light irradiation. O-phenylphenol (OPP) is widely used as fungicide and disinfectant, which may trigger growth-disturbing, genotoxicity in living organisms and kidney damage, serious threats the ecosystem and human health [34,35]. However, the photocatalytic degradation of OPP has rarely been investigated, especially under visible-light [36]. As shown in Fig. S5, prior to illumination, the adsorption-desorption equilibrium of the pollutant on the catalyst powders has been achieved for 60 min absorption process under magnetic stirring. As displayed in Fig. 9a, with prolonging the irradiation time, the characteristic absorbance of OPP at 243 nm and 282 nm declines promptly. After 120 min, it nearly vanishes in the present of Bi₄O₅Br₂ hollow spheres. Without photocatalyst, the OPP was hardly diminished under visible light irradiation (Fig. 9b). Under identical reaction for 120 min, only 19.1% OPP removal over the BiOBr nanosheets was observed, while the Bi₄O₅Br₂ nanosheets achieved a degradation efficiency of 39.6%. However, 88.5% and 99.4% removal ratios could be obtained for Bi₄O₅Br₂ layered microspheres and hollow spheres, indicating their excellent photocatalytic activity for OPP degradation under visible light. Fig. S6 demonstrates the HPLC chromatograms of OPP solution at varied reaction times in the presence of Bi₄O₅Br₂ LMs and HSS. It can be seen that OPP eluted at retention time of 4.55 min and rapidly declined with the increasing of irradiation time, which is consistent with the observation in UV-vis spectra. Therefore, it can be safely concluded that OPP can be effectively degraded by the Bi₄O₅Br₂ LMs and HSS under visible light irradiation.

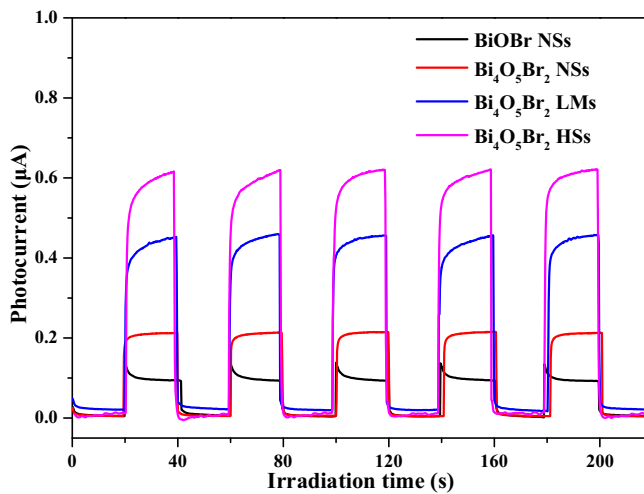


Fig. 11. The photocurrent responses of the as-prepared samples electrodes in 0.2 M Na₂SO₄ aqueous solution.

Provided that the OPP photodegradation process follows pseudo first-order decay kinetics, the calculated k value for Bi₄O₅Br₂ hollow spheres was estimated to be $3.51 \times 10^{-2} \text{ min}^{-1}$, which was 2.2 times than that ($1.59 \times 10^{-2} \text{ min}^{-1}$) of Bi₄O₅Br₂ layered microspheres, 7.9 times than that ($4.44 \times 10^{-3} \text{ min}^{-1}$) of Bi₄O₅Br₂ nanosheets and 19.7 times than that ($1.78 \times 10^{-3} \text{ min}^{-1}$) of BiOBr nanosheets (Fig. 9b). The structure parameters and photocatalytic activities of different samples were summarized in Table S1. To test the stability and reusability of the Bi₄O₅Br₂ layered microspheres and hollow spheres, the catalysts for the degradation of OPP were collected and recycled. As shown in Fig. S7, no appar-

ent deactivation of the two photocatalysts was observed after four continuous runs, which indicated that the as-prepared Bi₄O₅Br₂ layered microspheres and hollow spheres had a high catalytic stability, performing as genuine heterogeneous visible-light-induced photocatalysts for the removal of organic pollutants in wastewater.

In recent decades, the ubiquitous environmental issue of antibiotics has gained widespread attention [37]. The present of antibiotics in aquatic ecosystems may induce antibiotic resistance in microbial communities by inducing proliferation of bacterial drug resistance and chronic effects on aquatic organisms [38,39]. Therefore, it is imperative and significant to remove antibiotic agent from water. Norfloxacin (NOR) and tetracycline hydrochloride (TC) were chosen as two different type of model antibiotic agents to further confirm the photocatalytic ability of Bi₄O₅Br₂ layered microspheres and hollow spheres. As shown in Fig. 10, the NOR and TC self-photolysis could be neglected within the test period. It could be observed that Bi₄O₅Br₂ layered microspheres and hollow spheres exhibited much higher photocatalytic activity for the removal of NOR and TC than BiOBr and Bi₄O₅Br₂ nanosheets under visible light irradiation. As depicted in Fig. 10b, after 100 min of visible-light irradiation, 91.5% and 84.1% of NOR could be degraded by Bi₄O₅Br₂ hollow spheres and layered microspheres, while only 33.0% and 12.5% of NOR were degraded by Bi₄O₅Br₂ and BiOBr nanosheets, respectively. The calculated k value of Bi₄O₅Br₂ hollow spheres and layered microspheres for the degradation of NOR were higher than that of Bi₄O₅Br₂ and BiOBr nanosheets (Fig. 10c). As for the removal of TC, the similar trends during the photo-degradation process were also clearly observed (Fig. 10d-f). The results of photocatalytic degradation indicate the Bi-rich strategies and hollow structures can effectively improve photocatalytic activity of BiOBr for antibiotic agent removal.

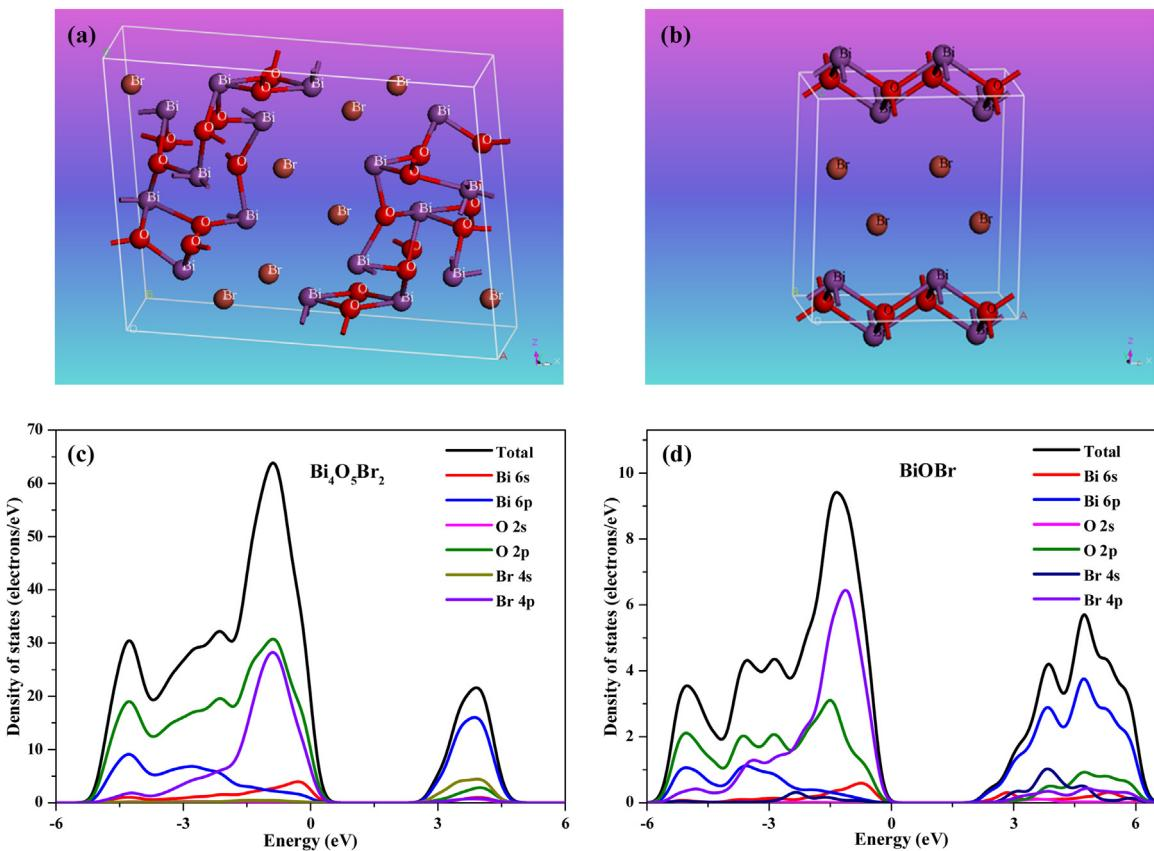


Fig. 12. Schematic representation of the crystal structures of Bi₄O₅Br₂ (a) and BiOBr (b); the calculated total DOS and partial DOS of Bi₄O₅Br₂ (c) and BiOBr (d).

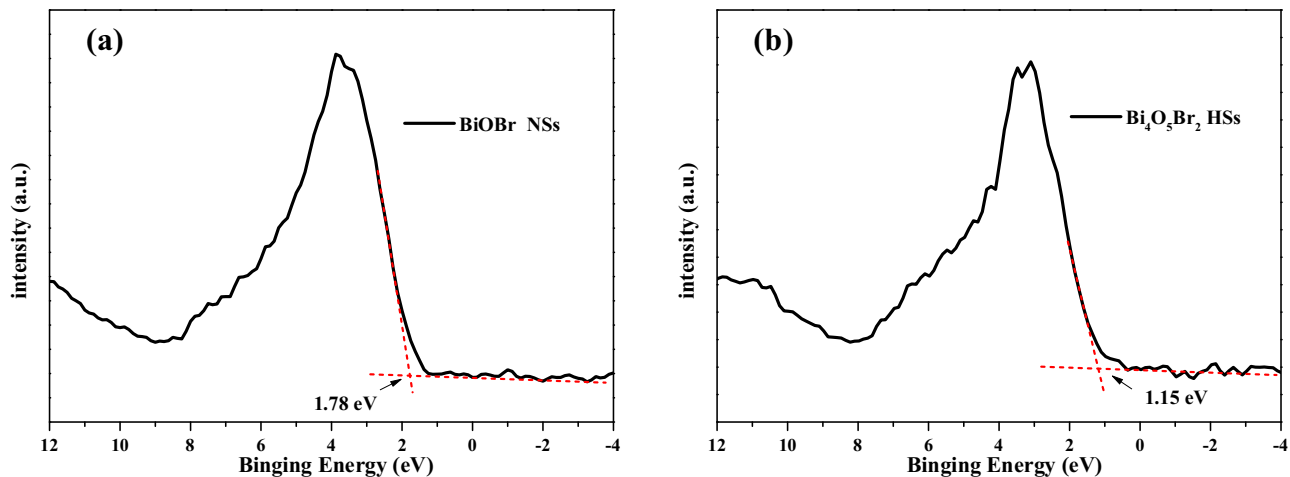


Fig. 13. XPS valence band spectra of the (a) BiOBr nanosheets and (b) Bi₄O₅Br₂ hollow spheres.

3.3. Photoelectrochemical activity

In order to provide further evidence to clarify the above photocatalytic performance, the transient photocurrent responses of all the material electrodes were recorded, which were verified to be useful tool to qualitatively study the separation and transfer efficiency of photo-induced charge carriers in photocatalysis [40]. Fig. 11 plots the transient photocurrent response for the BiOBr nanosheets compared to the Bi₄O₅Br₂ nanosheets, layered microspheres and hollow spheres. It can be seen that all the products show prompt and reproducible photocurrent responses in five on-off intermittent irradiation cycles. Meanwhile, the Bi₄O₅Br₂ hollow spheres display the highest current density among them, indicating the best charge separation and transfer efficiency of the photo-excited h⁺-e⁻ as well as longest lifetime of the charge carriers. The enhanced current density of Bi₄O₅Br₂ hollow spheres should be ascribed to the strong light scattering ability of the hollow layered structure with combined effects of its narrower band gap and more negative CB position [18,41–43].

3.4. Mechanism

To obtain further insight into the correlation of structure, morphology and property, the electronic structures of the Bi₄O₅Br₂

and BiOBr were theoretically calculated using plane-wave density function theory (DFT) with the CASTEP package. Fig. 12 displayed the crystal structure and calculated partial density of states (PDOS) of the Bi₄O₅Br₂ and BiOBr, respectively. It demonstrated that the valence band maximum (VBM) of BiOBr mainly consisted of Br 4p and O 2p orbitals, while the Bi 6p orbitals dominated the conduction band minimum (CBM). For bismuth-rich Bi₄O₅Br₂, although the composition of VBM and CBM is similar with that of BiOBr, the intensity of Bi 6p orbital in CB bottom of Bi₄O₅Br₂ is much stronger than that of BiOBr, resulting in a more negative conduction band [44,45]. Moreover, the XPS valence spectra can reflect the valence band of a semiconductor [46–48]. As shown in Fig. 13, the valence band with the maximum edge of the Bi₄O₅Br₂ hollow spheres and BiOBr nanosheets was measured to be 1.15 V and 1.78 V, respectively. Based on the results of optical measurements, the CB minimum of the Bi₄O₅Br₂ and BiOBr would occur at about -1.20 V and -0.97 V, respectively. Thus, the CB minimum of the Bi₄O₅Br₂ hollow spheres up-shifted by 0.23 V compared with that of BiOBr nanosheets, indicating that the E_{cb} of Bi₄O₅Br₂ was more negative than the E_{cb} of BiOBr, which was consistent with theoretical calculation results. Since the reduction potentials of •OH/OH⁻ and O₂/O₂⁻ are 2.3 and -0.33 V vs NHE, respectively, the Bi₄O₅Br₂ is unable to oxidize OH⁻ or water to generate •OH, yet it is feasible for Bi₄O₅Br₂ to trap molecular oxygen to generate O₂⁻. The above

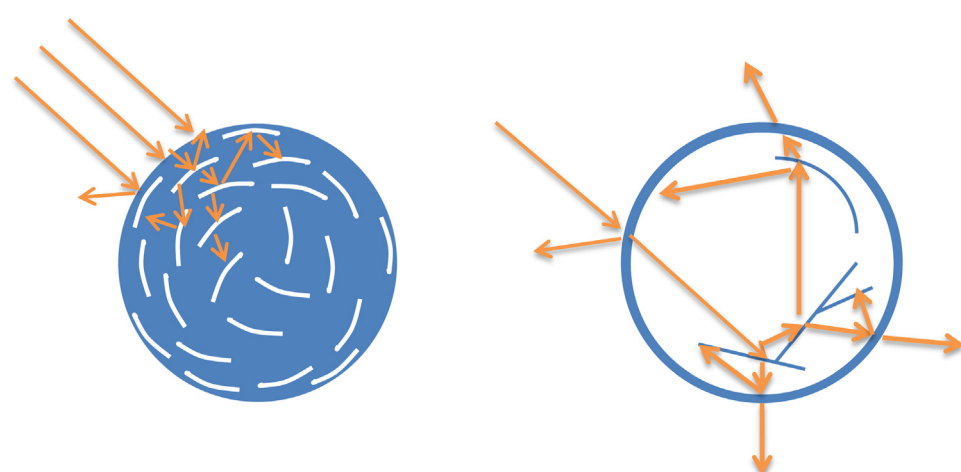


Fig. 14. Light reflection models in Bi₄O₅Br₂ layered microspheres and hollow spheres.

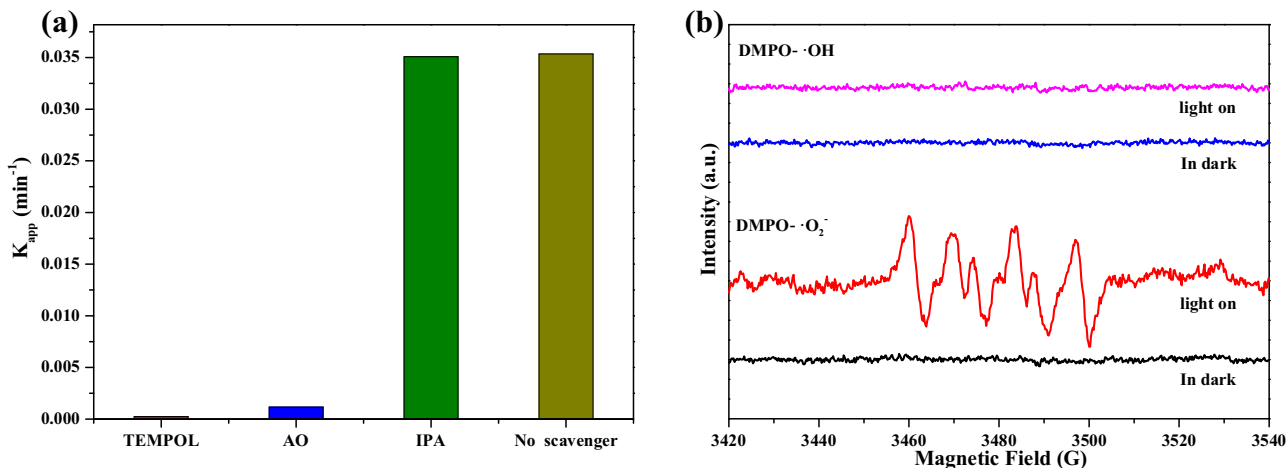


Fig. 15. (a) Photodegradation of OPP over $\text{Bi}_4\text{O}_5\text{Br}_2$ hollow spheres in the presence of different scavengers. (b) DMPO spin-trapping EPR spectra detected in methanol dispersion (for DMPO-glypH6O₂[−]) and aqueous dispersion (for DMPO-glypH6OH) under visible light irradiation with $\text{Bi}_4\text{O}_5\text{Br}_2$ hollow spheres.

results indicated that the more negative conduction band is an important factor resulting in the enhanced photocatalytic activity of $\text{Bi}_4\text{O}_5\text{Br}_2$ compared to BiOBr .

The $\text{Bi}_4\text{O}_5\text{Br}_2$ layered microspheres with relatively loose inside and hollow spheres exhibited the excellent photocatalytic ability owing to not only the crystal and band structures, but also the layered/hollow structure. The increased activity was primarily related to a more efficient light-harvesting, due to shorter diffusion length of charge carriers and multiple light reflections within their void space (Fig. 14), and high surface area that possesses more accessible catalytic centers. It is suggested to be another reason why the layered/hollow structures have excellent photocatalytic and photoelectrochemical performances.

To further verify and gain insight regarding the main active species responsible for the degradation of OPP on the $\text{Bi}_4\text{O}_5\text{Br}_2$ hollow spheres, we utilized ammonium oxalate (AO), isopropanol (IPA), 4-hydroxy-2,2,6,6-tetramethylpiperidinyloxy (TEMPOL) as h^+ , $\cdot\text{OH}$ and $\cdot\text{O}_2^-$ scavengers [49,50], respectively. As shown in Fig. 15a, compared with no scavenger system, the photodegradation efficiency of OPP over $\text{Bi}_4\text{O}_5\text{Br}_2$ hollow spheres remained almost the same after adding isopropanol. However, the addition of TEMPOL almost terminated the photodegradation reaction, indicating that $\cdot\text{O}_2^-$ was the crucial species for the degradation of OPP over $\text{Bi}_4\text{O}_5\text{Br}_2$ hollow spheres. As for the AO-photocatalysis system, an obvious inhibition was observed, which confirms h^+ was another main active species. Meanwhile, EPR spin-trap technique was conducted to further confirm the existence of $\cdot\text{OH}$ and $\cdot\text{O}_2^-$ radicals generated over $\text{Bi}_4\text{O}_5\text{Br}_2$ hollow spheres under visible light irradiation. As presented in Fig. 15b, strong DMPO- $\cdot\text{O}_2^-$ signals were observed after visible light irradiation, confirming that the photo-generated electrons (e^-) on the CB of $\text{Bi}_4\text{O}_5\text{Br}_2$ could be trapped to produce $\cdot\text{O}_2^-$. Therefore, the photodegradation of OPP over the $\text{Bi}_4\text{O}_5\text{Br}_2$ hollow structures under visible light was likely to be dominated by $\cdot\text{O}_2^-$ radical and directed h^+ oxidation. The photocatalytic mechanism is in accordance with the above analysis of the band structure of $\text{Bi}_4\text{O}_5\text{Br}_2$.

4. Conclusion

In summary, a facile and one-step microemulsion-mediated method was presented for the synthesis of Bi-rich $\text{Bi}_4\text{O}_5\text{Br}_2$ with controllable morphologies of 2D nanosheets, 3D monodisperse layered microspheres and hollow spheres. The surfactant TX-100 acts as the stabilizer of Br-containing ternary microemulsion, and its concentration plays an important role in the formation of $\text{Bi}_4\text{O}_5\text{Br}_2$

with different morphologies. To the best of our knowledge, it is the first research on synthesis of $\text{Bi}_4\text{O}_5\text{Br}_2$ with the shape of monodisperse layered microspheres and hollow spheres. The $\text{Bi}_4\text{O}_5\text{Br}_2$ layered microspheres and hollow spheres displayed higher photocatalytic activity than BiOBr nanosheets for the degradation of OPP, NOR and TC under visible light irradiation, which can be attributed to the combined effect of the crystal and band structures, more negative conduction band position and hollow morphology with large specific surface area and multiple light-scattering. In addition, the results of scavenger experiment and EPR analysis indicate that $\cdot\text{O}_2^-$ and h^+ are the main active species during the visible-light photocatalytic process. This work demonstrated a feasible soft-template route to synthesize morphology-tunable Bi-rich Bi-O-X and some insight for the fabrication of highly efficient visible-light-induced photocatalysts.

Acknowledgement

This work was financially supported by National Natural Science Foundation of China (Nos. 51578279 and 51278242).

Appendix A. Supplementary data

Supplementary data associated with this article can be found, in the online version, at <http://dx.doi.org/10.1016/j.apcatb.2017.02.010>.

References

- [1] J. Yan, G. Wu, N. Guan, L. Li, *Appl. Catal. B Environ.* 152–153 (2014) 280–288.
- [2] Z.F. Jiang, C.Z. Zhu, W.M. Wan, K. Qian, J.M. Xie, *J. Mater. Chem. A* 4 (2016) 1806–1818.
- [3] X. Xiao, C.L. Xing, G.P. He, X.X. Zuo, J.M. Nan, L.S. Wang, *Appl. Catal. B Environ.* 148–149 (2014) 154–163.
- [4] Z.G. Zou, J.H. Ye, K. Sayama, H. Arakawa, *Nature* 414 (2001) 625–627.
- [5] A. Kudo, Y. Miseki, *Chem. Soc. Rev.* 38 (2009) 253–278.
- [6] F.E. Osterloh, *Chem. Mater.* 20 (2008) 35–54.
- [7] Y.N. Huo, R.J. Hou, X.F. Chen, H.B. Yin, Y. Gao, H.X. Li, *J. Mater. Chem. A* 3 (2015) 14801–14808.
- [8] S.N. Xiao, W. Zhu, P.J. Liu, F.F. Liu, W.R. Dai, D.Q. Zhang, W. Chen, H.X. Li, *Nanoscale* 8 (2016) 2899–2907.
- [9] H. Zhang, J. Sun, V.L. Dagle, B. Halevi, A.K. Datye, Y. Wang, *ACS Catal.* 4 (2014) 2379–2386.
- [10] K.L. Zhang, C.M. Liu, F.Q. Huang, C. Zheng, W.D. Wang, *Appl. Catal. B: Environ.* 68 (2006) 125–129.
- [11] D.Q. Zhang, M.C. Wen, B. Jiang, G.S. Li, Jimmy C. Yu, *J. Hazard. Mater.* 211–212 (2012) 104–111.
- [12] D. Mao, X.M. Lü, Z.F. Jiang, J.M. Xie, X.F. Lu, W. Wei, A.M. Showkat Hossain, *Mater. Lett.* 118 (2014) 154–157.
- [13] L. Ye, Y. Su, X. Jin, H. Xie, C. Zhang, *Environ. Sci.: Nano* 1 (2014) 90–112.

[14] L. Kong, Z. Jiang, H.H. Lai, R.J. Nicholls, T.C. Xiao, M.O. Jones, P.P. Edwards, *J. Catal.* 293 (2012) 116–125.

[15] Y.N. Huo, J. Zhang, M. Miao, Y. Jin, *Appl. Catal. B: Environ.* 111–112 (2012) 334–341.

[16] H.W. Huang, X. Han, X.W. Li, S.C. Wang, P.K. Chu, Y.H. Zhang, *ACS Appl. Mater. Interfaces* 7 (2015) 482–492.

[17] Y.X. Guo, H.W. Huang, Y. He, N. Tian, T.R. Zhang, P.K. Chu, Q. An, Y.H. Zhang, *Nanoscale* 7 (2015) 11702–11711.

[18] J.L. Wang, Y. Yu, L.Z. Zhang, *Appl. Catal. B: Environ.* 136–137 (2013) 112–121.

[19] L.Q. Ye, X. Jin, C. Liu, C. Ding, H. Xie, K.H. Chu, P.K. Wong, *Appl. Catal. B: Environ.* 187 (2016) 281–290.

[20] H. Deng, J. Wang, Q. Peng, X. Wang, Y.D. Li, *Chem. Eur. J.* 11 (2005) 6519–6524.

[21] X.L. Jin, L.Q. Ye, H. Wang, Y.R. Su, H.Q. Xie, Z.G. Zhong, H. Zhang, *Appl. Catal. B: Environ.* 165 (2015) 668–675.

[22] X. Xiao, R. Hu, C. Liu, C. Xing, X. Zuo, J. Nan, L. Wang, *Chem. Eur. J.* 225 (2013) 790–797.

[23] J.X. Xia, M.X. Ji, J. Di, B. Wang, S. Yin, Q. Zhang, M.Q. He, H.M. Li, *Appl. Catal. B Environ.* 191 (2016) 235–245.

[24] J.X. Xia, J. Di, H.T. Li, H. Xu, H.M. Li, S.J. Guo, *Appl. Catal. B: Environ.* 181 (2016) 260–269.

[25] Y.N. Wang, K.J. Deng, L.Z. Zhang, *J. Phys. Chem. C* 115 (2011) 14300–14308.

[26] J. Di, J.X. Xia, M.X. Ji, B. Wang, S. Yin, Q. Zhang, Z.G. Chen, H.M. Li, *Appl. Catal. B Environ.* 183 (2016) 254–262.

[27] S.H. Tu, M.L. Lu, X. Xiao, C.X. Zheng, H. Zhong, X.X. Zuo, J.M. Nan, *RSC Adv.* 6 (2016) 44552–44560.

[28] J. Di, J.X. Xia, M.X. Ji, S. Yin, H.P. Li, H. Xu, Q. Zhang, H.M. Li, *J. Mater. Chem. A* 3 (2015) 15108–15118.

[29] Z.X. Wang, M. Chen, L.M. Wu, *Chem. Mater.* 20 (2008) 3251–3253.

[30] S.H. Zhang, Y.N. Gao, B. Dong, L.Q. Zheng, *Colloids Surf. A: Physicochem. Eng. Aspects* 372 (2010) 182–189.

[31] Y.N. Gao, S.B. Han, B.X. Han, G.Z. Li, D. Shen, Z.H. Li, J.M. Du, W.G. Hou, G.Y. Zhang, *Langmuir* 21 (2005) 5681–5684.

[32] Z.F. Jiang, W. Wei, D.J. Mao, C. Chen, Y.F. Shi, X.M. Lv, J.M. Xie, *Nanoscale* 7 (2015) 784–797.

[33] L.Q. Ye, X.L. Jin, C. Liu, C.H. Ding, H.Q. Xie, K.H. Chu, P.K. Wong, *Appl. Catal. B: Environ.* 187 (2016) 281–290.

[34] H. Wei, Y.P. Hang, Y.D. Zhu, C.L. Song, *Anal. Methods* 7 (2015) 5593–5599.

[35] N. Kolbe, J.T. Andersson, J. Agric. Food Chem. 54 (2006) 5736–5741.

[36] R.P. Hu, X. Xiao, S.H. Tu, X.X. Zuo, J.M. Nan, *Appl. Catal. B: Environ.* 163 (2015) 510–519.

[37] M.B. Feng, X.H. Wang, J. Chen, R.J. Qu, Y.X. Sui, L. Cizmas, Z.Y. Wang, V.K. Sharma, *Water Res.* 103 (2016) 48–57.

[38] T.C. An, H. Yang, G.Y. Li, W.H. Song, W.J. Cooper, X.P. Nie, *Appl. Catal. B: Environ.* 94 (2010) 288–294.

[39] X.V. Doorslaer, K. Demeestere, P.M. Heynderickx, H.V. Langenhove, J. Dewulf, *Appl. Catal. B: Environ.* 101 (2011) 540–547.

[40] Z.F. Jiang, D.L. Jiang, Z.X. Yan, D. Liu, K. Qian, J.M. Xie, *Appl. Catal. B: Environ.* 170–171 (2015) 195–205.

[41] Z. Wang, J.G. Hou, C. Yang, S.Q. Jiao, K. Huang, H.M. Zhu, *Energy Environ. Sci.* 6 (2013) 2134–2144.

[42] W. Guo, Q. Qin, L. Geng, D. Wang, Y.H. Guo, Y.X. Yang, *J. Hazard. Mater.* 308 (2016) 374–385.

[43] G.J. Ke, H.Y. Chen, C.Y. Su, D.B. Kuang, *J. Mater. Chem. A* 1 (2013) 13274–13282.

[44] J. Shang, W.C. Hao, X.J. Lv, T.M. Wang, X.L. Wang, Y. Du, S.X. Dou, T.F. Xie, D.J. Wang, J. Wang, *ACS Catal.* 4 (2014) 954–961.

[45] C.Y. Wang, X. Zhang, X.N. Song, W.K. Wang, H.Q. Yu, *ACS Appl. Mater. Interfaces* 8 (2016) 5320–5326.

[46] J. Pan, X. Wu, L. Wang, G. Liu, G. Lu, H. Cheng, *Chem. Commun.* 47 (2011) 8361–8363.

[47] L. Sun, X. Zhao, C. Jia, Y. Zhou, X. Cheng, P. Li, L. Liu, W. Fan, *J. Mater. Chem.* 22 (2012) 23428–23438.

[48] S. Yan, Z. Wang, Z. Li, Z. Zou, *J. Mater. Chem.* 21 (2011) 5682–5686.

[49] D.J. Mao, A.Q. Yu, S.S. Ding, F. Wang, S.G. Yang, C. Sun, H. He, Y.Z. Liu, K. Yu, *Appl. Surf. Sci.* 349 (2015) 957–969.

[50] G.P. He, C.L. Xing, X. Xiao, R.P. Hu, X.X. Zuo, J.M. Nan, *Appl. Catal. B: Environ.* 170–171 (2015) 1–9.